

# Dust distributions in the Magellanic Clouds

B.-Q. Chen,<sup>1\*</sup> H.-L. Guo,<sup>1\*</sup> J. Gao,<sup>2\*</sup> M. Yang,<sup>3</sup> Y.-L. Liu,<sup>1</sup> and B.-W. Jiang<sup>2</sup>

<sup>1</sup>South-Western Institute for Astronomy Research, Yunnan University, Kunming, 650500, P. R. China

<sup>2</sup>Department of Astronomy, Beijing Normal University, Beijing, 100875, P. R. China

<sup>3</sup>IAASARS, National Observatory of Athens, Vas. Pavlou and I. Metaxa, Penteli 15236, Greece

Accepted ???, Received ???; in original form ???

## ABSTRACT

We present high-resolution maps of the dust reddening in the Magellanic Clouds (MCs). The maps cover the Large and Small Magellanic Cloud (LMC and SMC) area and have a spatial angular resolution between  $\sim 26$  arcsec and 55 arcmin. Based on the data from the optical and near-infrared (IR) photometric surveys, including the Gaia Survey, the SkyMapper Southern Survey (SMSS), the Survey of the Magellanic Stellar History (SMASH), the Two Micron All Sky Survey (2MASS) and the near-infrared  $YJK_S$  VISTA survey of the Magellanic Clouds system (VMC), we have obtained multi-band photometric stellar samples containing over 6 million stars in the LMC and SMC area. Based on the measurements of the proper motions and parallaxes of the individual stars from Gaia Early Data Release 3 (Gaia EDR3), we have built clean samples that contain stars from the LMC, SMC and Milky Way (MW), respectively. We apply the spectral energy distribution (SED) fitting to the individual sample stars to estimate their reddening values. As a result, we have derived the best-fitting reddening values of  $\sim 1.9$  million stars in the LMC, 1.5 million stars in the SMC and 0.6 million stars in the MW, which are used to construct dust reddening maps in the MCs. Our maps are consistent with those from the literature. The resultant high-resolution dust maps in the MCs are not only important tools for reddening correction of sources in the MCs, but also fundamental for the studies of the distribution and properties of dust in the two galaxies.

**Key words:** dust, extinction – Magellanic Clouds – ISM: structure

## 1 INTRODUCTION

The Magellanic Clouds (MCs), comprising the Large and Small Magellanic Clouds (LMC and SMC), are the largest satellite galaxies orbiting our Milky Way (MW) galaxy. They serve as excellent astrophysical laboratories for the studies of the stellar populations, structure and assembly history of dwarf irregular galaxies. Mapping the dust distribution in the MCs are fundamental for both the reddening corrections of sources in the MCs and the studies of the structure and properties of the dust in the two galaxies.

In the last few decades, many attempts have been carried out to map the distribution of reddening and dust in the MCs. We hereby only mention a few of these works. Harris et al. (1997) presented a reddening map of the LMC based on 2,069 O and B main sequence stars selected from the *UBVI* Magellanic Cloud Photometric Survey (Zaritsky et al. 1997). Based on the catalogue from the Magellanic Cloud Photometric Survey, Zaritsky et al. (2002, 2004) presented the extinction maps of the SMC and the LMC, respectively. Subramaniam (2005) presented a  $E(V - I)$  reddening map of the LMC bar based on the red clump stars selected from the Optical Gravitational Lensing Experiment II (OGLE-II; Udalski et al. 2000). Based on the near-IR photometric data from the Two Micron All-Sky Survey (2MASS; Skrutskie et al. 2006), Dobashi et al. (2008, 2009) presented dust maps of the LMC and the SMC, respectively. The maps

have a resolution of 2.6 arcmin. Pejcha & Stanek (2009) presented a reddening map of the LMC based on  $\sim 9000$  RR Lyrae stars selected from the OGLE-III catalogue (Soszyński et al. 2009). Their map has a resolution of  $0.2^\circ$ . Choi et al. (2018) presented a  $E(g - i)$  reddening map which covers  $165 \text{ deg}^2$  of the LMC disk with a resolution of  $\sim 10$  arcmin based on  $\sim 2$  million red clump stars selected from the Survey of the MAGellanic Stellar History (SMASH; Nidever et al. 2017). Joshi & Panchal (2019) presented reddening maps of the MCs based on  $\sim 8000$  Cepheids selected from the OGLE-IV photometric survey (Udalski et al. 2015). The maps have resolutions of about  $1.2 \text{ deg}^2$  and  $0.22 \text{ deg}^2$  for the LMC and SMC, respectively. Górski et al. (2020) presented reddening maps of the MCs with a spatial resolution of 3 arcmin based on the OGLE-III red clump stars. Skowron et al. (2021) presented reddening maps of the MCs based on the OGLE-IV red clump stars. The resolution of their map varies between 1.7 and 27 arcmin.

The dust maps of the MCs show a highly inhomogeneous clumpy distribution. To accurately correct the extinction effect of objects in MCs, high-resolution maps are always welcome. The resolution of an extinction map is usually determined by the density of the tracer. Most of the previous works map the dust distributions in the MCs using a certain type of tracer in the MCs, such as the RR Lyrae stars (e.g. Pejcha & Stanek 2009; Haschke et al. 2011; Deb 2017), Cepheids (e.g. Inno et al. 2016; Joshi & Panchal 2019) or red clump stars (e.g. Subramaniam 2005; Subramanian & Subramanian 2012; Haschke et al. 2011; Tatton et al. 2013; Choi et al. 2018; Górski et al.

\* E-mail: bchen@ynu.edu.cn (BQC); helong\_guo@mail.ynu.edu.cn (HLG); jiangao@bnu.edu.cn (JG).

2020; Skowron et al. 2021). Their sample sizes are relatively small, which further limit the resolutions of the resultant reddening maps.

To study the structures and properties of the dust in the LMC and SMC themselves, one needs to consider the contamination of the Galactic foreground dust. As the MCs are located at high Galactic latitudes ( $b \sim -33^\circ$  for LMC and  $-44^\circ$  for SMC), previous works usually ignore the foreground dust contamination of the MW. However, as shown in the recent three-dimensional dust map of the southern sky (Guo et al. 2021), there are clear Galactic foreground dust clouds toward the LMC and SMC area. The contamination of the foreground MW dust should be carefully considered when studying the dust properties in the MCs.

In the current work, we collect data from several optical and near-infrared (IR) photometric surveys that cover the MCs, and build multi-band photometric stellar samples of over 6 million stars. Based on the robust measurements of stellar proper motions and parallaxes from Gaia Early Data Release 3 (Gaia EDR3; Gaia Collaboration et al. 2021a), we have obtained clean samples that contain stars from the LMC, SMC and MW, respectively. We apply spectral energy distribution (SED) fitting to the individual sample stars and obtained robust reddening values of about 4 million stars. We then construct high-resolution dust reddening maps of the MCs. The inhomogeneous Galactic foreground dust distribution in the regions toward the MCs are also mapped and been excluded to obtain the local dust maps of the MCs.

This paper is structured as follows. In Sect 2, we introduce the data used in this paper. In Sect 3, we describe our method. The results are presented in Sect 4 and discussed in Sect. 5. Finally, we summarize in Sect 6.

## 2 DATA

Our work is based on the optical and near-IR photometries from several multi-band photometric surveys that cover the MCs, including the Gaia Survey, SkyMapper Southern Survey (SMSS; Keller et al. 2007), SMASH, 2MASS and the near-infrared  $YJK_S$  VISTA survey of the Magellanic Clouds system (VMC; Cioni et al. 2011).

The Gaia EDR3 was released in 2020. It provides high precision celestial positions and  $G$  broad-band photometric measurements for  $\sim 1.8$  billion sources. Among them,  $\sim 1.5$  billion sources have parallaxes, proper motions, the  $G_{BP}$  and  $G_{RP}$  magnitudes. The typical uncertainties of the parallax and proper motion measurements are 0.5 mas at  $G = 20$  mag. For the mean  $G$ -,  $G_{BP}$ - and  $G_{RP}$ -band photometries, the typical uncertainties are 6, 108 and 52 mmag at  $G = 20$  mag (Gaia Collaboration et al. 2021a).

The SMSS surveys the southern sky in six optical filters:  $u$ ,  $v$ ,  $g$ ,  $r$ ,  $i$  and  $z$ , using the 1.35 m SkyMapper Telescope located at Siding Spring Observatory. The SkyMapper Imager CCD mosaic contains  $32\,2048 \times 4096$  CCDs, with a pixel scale of  $\sim 0.5''$  and a total field-of-view of  $2.4 \times 2.3$  deg $^2$ . In the current work we use the SMSS Second Data Release (SMSS DR2; Onken et al. 2019), which was released in 2020. As measured by internal reproducibility, the photometry has a precision of 1 per cent in  $u$  and  $v$ , and 0.7 per cent in  $g$ ,  $r$ ,  $i$  and  $z$  (Onken et al. 2019).

The SMASH survey used the Dark Energy Camera (DECam; Flaugher et al. 2015) on the Blanco 4 m Telescope at Cerro Tololo Inter-American Observatory (CTIO). The DECam contains  $62\,2k \times 4k$  CCDs, with a pixel scale of  $0.263''$ . The SMASH survey has five optical bands:  $u$ ,  $g$ ,  $r$ ,  $i$  and  $z$ . In the current work, we use the Second Data Release of SMASH (SMASH DR2; Nidever et al. 2021), which was released in 2020. The SMASH DR2 contains  $\sim 4$

billion measurements of  $\sim 360$  million objects. The photometry has a precision of about 1 per cent in  $u$  and 0.5 to 0.7 per cent in  $g$ ,  $r$ ,  $i$  and  $z$ .

The 2MASS survey used two 1.3 m telescopes respectively located at Mt. Hopkins and CTIO. Each telescope is equipped with three-channel cameras using  $256 \times 256$  arrays of HgCdTe detectors. 2MASS has three near-IR bands:  $J$ ,  $H$  and  $K_S$ . In the current work we use the 2MASS Point Source Catalog (2MASS PSC; Skrutskie et al. 2006). The 2MASS photometric systematic uncertainties are smaller than 0.03 mag.

The VMC surveyed a total area of  $\sim 170$  deg $^2$  toward the MCs in three near-IR filters:  $Y$ ,  $J$  and  $K_S$ , using the 4.1 m Visible and Infrared Survey Telescope for Astronomy (VISTA; Emerson et al. 2004) located at the Paranal Observatory. The  $10\sigma$  limiting magnitudes of VMC are  $\sim 21.1$ , 21.3 and 20.7 mag respectively in the  $Y$ ,  $J$  and  $K_S$  bands. In the current work we use the VMC Data Release 5.1 (VMC DR5.1; Rubele et al. 2018), which was released in 2020. The VMC DR5.1 contains 14.6 million sources toward the SMC, the Magellanic Bridge and the Magellanic Stream. For the LMC area, we adopt the VMC Data Release 4 (VMC DR4; Rubele et al. 2012), which provides  $YJK_S$  photometries of sources in several fields of the LMC.

In this work, we will apply the SED fitting algorithm to the multi-band photometric data of the individual stars to calculate their reddening values. To break the degeneracy between the stellar intrinsic colours and their reddening values (Bailer-Jones 2011; Berry et al. 2012), we combine the optical observations of the individual stars (Gaia EDR3, SMSS DR2, SMASH DR2) with their near-IR data (2MASS PSC, VMC DR4 or DR5.1). In addition, we adopt the Gaia EDR3 astrometric measurements to distinguish the LMC or SMC stars from the MW stars.

We first select stars located in the MCs area from the Gaia EDR3. In the current work, we define the area with right ascension (RA) between  $4^h$  and  $7^h$  and declination (Dec) between  $-78^\circ$  and  $-60^\circ$  as the LMC area, and that with RA between  $0^h$  and  $2^h$  and Dec between  $-78^\circ$  and  $-68^\circ$  as the SMC area. We then cross-match the Gaia EDR3 stars with the optical and near-IR catalogues, respectively, using a matching radius of 1.5 arcsec. We require that the sources must have detections in both the optical bands ( $gri$  of SMSS DR2 or SMASH DR2) and the near-IR bands ( $JHK_S$  of 2MASS PSC or  $YJK_S$  of the VMC DR4 and DR5.1). As a result, we have obtained four different multi-band photometric samples: the Gaia/SMSS/2MASS (GS2) sample, the Gaia/SMSS/VMC (GSV) sample, the Gaia/SMASH/2MASS (GM2) sample, and the Gaia/SMASH/VMC (GMV) sample. For each sample, we require that the sources must be detected in eight bands: Gaia  $G_{BP}G_{RP}$ , SMSS/SMASH  $gri$  and 2MASS  $JHK_S$ /VMC  $YJK_S$ , and their photometric errors in all eight bands are less than 0.1 mag. These cuts lead to 845,930, 848,984, 614,648, and 4,367,440 stars in the GS2, GSV, GM2, and GMV catalogue, respectively. For all the SMASH, SMSS, 2MASS and VMC bands, the errors of stars with reported photometric uncertainties less than 0.02 mag are reset to 0.02 mag, which is to account for plausible calibration uncertainties. The value of 0.02 mag comes from the systematic errors of the 2MASS photometry (Skrutskie et al. 2006). Since we will use the empirical stellar SED libraries (Sect. 3) in the current work, we can then ignore any effects from the zero-point calibrations of the various systems. The spatial distributions of the individual stars in the four catalogues are shown in Fig. 1.

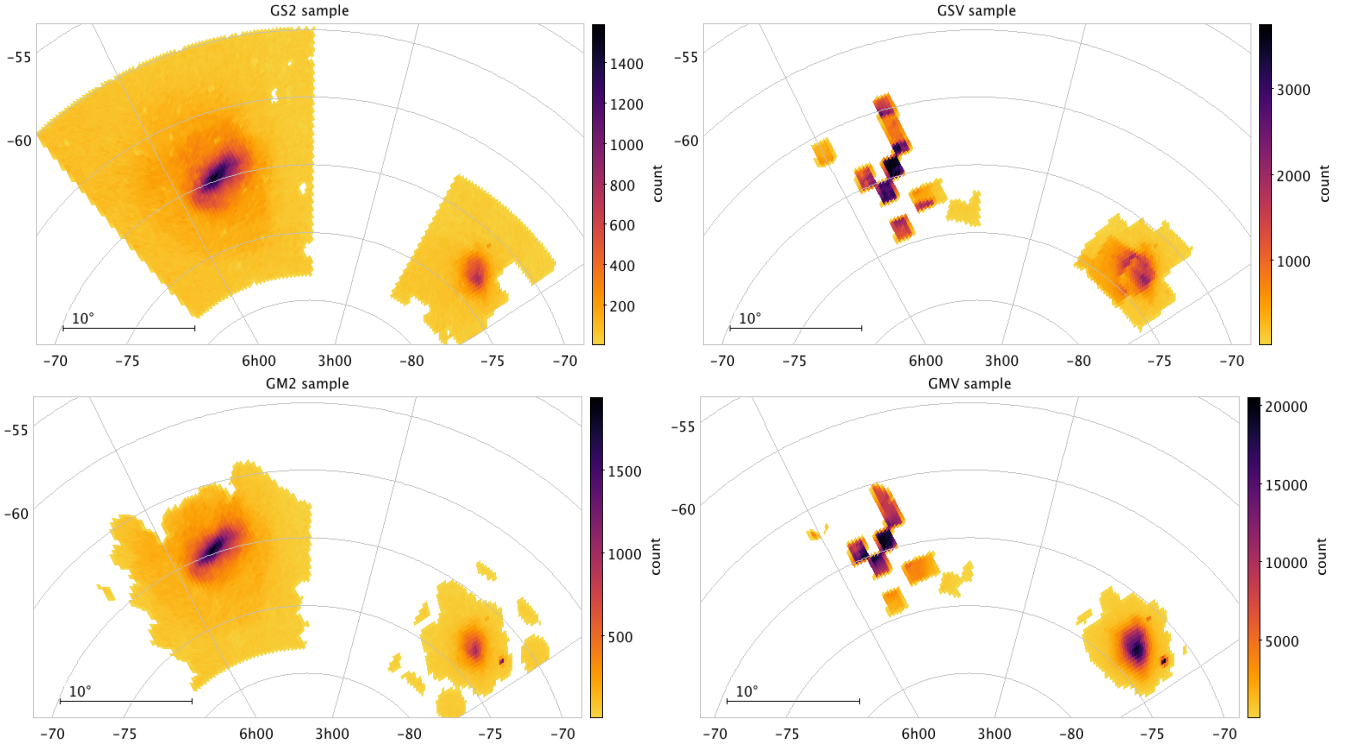


**Figure 1.** Spatial distributions of stars from the individual catalogues. Different colours represent number of stars in bins of  $0.05 \text{ deg}^2$  size.

### 3 METHOD

#### 3.1 The LMC, SMC and MW samples

We first establish clean source catalogues of stars respectively from the LMC, SMC and MW. We adopt a method similar to that used by Yang et al. (2019, 2021) and Gaia Collaboration et al. (2021b). The Gaia EDR3 astrometric measurements (Gaia Collaboration et al. 2021a) are used to determine the membership of LMC and SMC stars. Fig. 2 shows the selections of the LMC and SMC stars in this work. We select only stars with parallax and proper motions within the  $3\sigma$  limits of LMC and SMC, respectively. We adopt the mean and dispersion values of the astrometry of the LMC and SMC stars from Gaia Collaboration et al. (2021b). For LMC star selection, we adopt the criteria: proper motion in RA  $0.4192 < PM_{\text{RA}} < 3.1024 \text{ mas/yr}$ , proper motion in Dec  $-1.6087 < PM_{\text{Dec}} < 2.2163 \text{ mas/yr}$  and parallax  $-1.0078 < \varpi < 0.9998 \text{ mas}$ . For SMC, we adopt the criteria:  $-0.3863 < PM_{\text{RA}} < 1.8505 \text{ mas/yr}$ ,  $-2.1232 < PM_{\text{Dec}} < -0.3280 \text{ mas/yr}$  and  $-0.9845 < \varpi < 0.9793 \text{ mas}$ . In addition, we have removed stars with proper motion errors larger than  $0.5 \text{ mas/yr}$  and parallax errors larger than  $0.5 \text{ mas}$ . As a result, we have obtained a total of  $\sim 3$  million LMC stars and 1.7 million SMC stars from the four multi-band photometric stellar catalogues mentioned in Sect. 2.

We have also selected a clean MW star sample using the criteria:  $\varpi > 0.2 \text{ mas}$ , parallax error  $0 < \sigma_{\varpi} < 0.1 \text{ mas}$  and the relative uncertainty of parallax  $\sigma_{\varpi}/\varpi < 0.2$ . This yields a total of  $\sim 0.7$  million MW stars in the LMC and SMC areas. We note that we have adopted very strict constraints when we select the Galactic foreground stars. We have excluded any stars locating at distances larger than  $5 \text{ kpc}$  from the Sun or having large parallax errors. This is because that we want to select a Galactic foreground star sample as clean as possible. The Gaia EDR3 parallaxes of sources located at distances  $d > 5 \text{ kpc}$  from the Sun usually suffer larger uncertainties. As the MCs are located at high Galactic latitudes, the dust from the

**Table 1.** The extinction coefficient for all passbands adopted in the current work.

Filter	Effective wavelength ( $\text{\AA}$ )	$R_V$		
		MW	LMC	SMC
Gaia $G_{\text{BP}}$	5182.58 <sup>a</sup>	3.324	3.639	2.960
Gaia $G_{\text{RP}}$	7825.08 <sup>a</sup>	1.932	2.179	1.645
SMASH $g$	4841.88 <sup>b</sup>	3.628	3.943	3.263
SMASH $r$	6438.53 <sup>b</sup>	2.595	2.880	2.263
SMASH $i$	7821.01 <sup>b</sup>	1.933	2.181	1.646
SMSS $g$	5099.44 <sup>c</sup>	3.392	3.707	3.027
SMSS $r$	6157.28 <sup>c</sup>	2.731	3.025	2.390
SMSS $i$	7778.37 <sup>c</sup>	1.953	2.201	1.665
VMC $Y$	10573.79 <sup>d</sup>	1.145	1.307	0.956
VMC $J$	21771.24 <sup>d</sup>	0.845	0.964	0.705
VMC $K_S$	21475.88 <sup>d</sup>	0.366	0.418	0.305
2MASS $J$	12357.60 <sup>e</sup>	0.889	1.015	0.742
2MASS $H$	16476.02 <sup>e</sup>	0.561	0.640	0.468
2MASS $K_S$	21620.75 <sup>e</sup>	0.362	0.413	0.302

Note: <sup>a</sup>Riello et al. (2021), <sup>b</sup>Abbott et al. (2018), <sup>c</sup>Bessell (2011), <sup>d</sup>Dalton et al. (2006), <sup>e</sup>Cohen et al. (2003).

MW mainly locates at close distances ( $d < 1 \text{ kpc}$ ; Chen et al. 2013; Schultheis et al. 2014; Chen et al. 2019; Green et al. 2019). We can then use our selected MW stars to map the Galactic foreground dust distribution of the regions toward the MCs.

In Fig. 3 we show the Gaia  $G_{\text{BP}} - G_{\text{RP}}$  versus  $G$  colour-magnitude diagram of our selected LMC, SMC and MW stars from the GMV catalogue. Based on the astrometric constraints, we are able to obtain clean LMC, SMC and MW stellar samples.



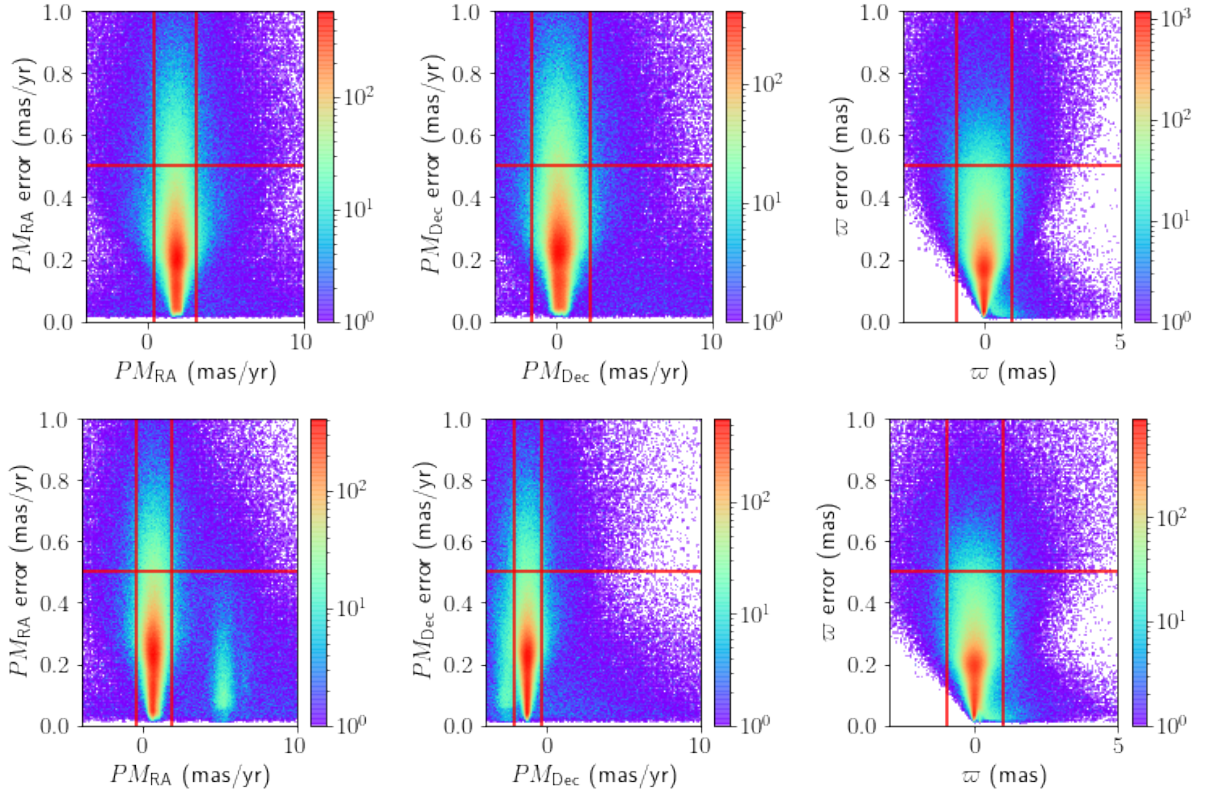


**Figure 2.** The selection of clean LMC (upper panels) and SMC (bottom panels) source samples for the GMV catalogue. From left to right of each row show the Gaia EDR3 proper motions in RA, Dec and parallaxes plotted against their errors. The red lines show the criteria adopted to select LMC and SMC stars in the current work.

**Table 2.** Parameters of the reference samples.

Sample	$E(B - V)_{\max}$ mag	N	$(g - K_S)_{0,\min}$ mag	$(g - K_S)_{0,\max}$ mag
GS2-LMC	0.050	14,219	-0.2	5.7
GS2-SMC	0.055	9,500	-0.8	7.2
GS2-MW	0.035	38,977	-0.1	6.2
GSV-LMC	0.035	10,001	-1.0	5.3
GSV-SMC	0.035	15,949	-1.0	6.2
GSV-MW	0.035	13,278	0.5	5.8
GM2-LMC	0.065	9,739	0.5	5.7
GM2-SMC	0.055	9,305	1.2	7.8
GM2-MW	0.045	12,831	0.8	6.2
GMV-LMC	0.055	14,504	-1.0	5.8
GMV-SMC	0.035	124,802	-1.0	8.0
GMV-MW	0.030	12,415	-1.0	6.7

### 3.2 Reddening determinations for the individual stars

In this work, we adopt a SED fitting algorithm similar to that of Berry et al. (2012), Chen et al. (2014) and Guo et al. (2021) to the multi-band photometric data of the individual stars to calculate their reddening values. For a given star, we simulate its observed colour of bands  $\lambda_1$  and  $\lambda_2$  by,

$$c_{\text{sim}} = c_{\text{sl}}[(g - K_S)_0] + (R_{\lambda_1} - R_{\lambda_2}) \cdot E(B - V), \quad (1)$$

where the intrinsic colour  $(g - K_S)_0$  and reddening value  $E(B - V)$  are free parameters to fit.  $c_{\text{sim}}$  is the simulated color of bands  $\lambda_1$  and  $\lambda_2$  for the star and  $c_{\text{sl}}[(g - K_S)_0]$  the corresponding intrinsic color pre-

dicted by the reference stellar locus for given  $(g - K_S)_0$ .  $R_{\lambda_1}$  and  $R_{\lambda_2}$  are the extinction coefficients of bands  $\lambda_1$  and  $\lambda_2$ , respectively. For the extinction law, we adopt the results from Gordon et al. (2003). We assume  $R_V = 3.41, 2.74$  and  $3.1$  for the LMC, SMC and MW respectively. The Cardelli, Clayton & Mathis (1989)  $R_V$ -dependent extinction curves are adopted to obtain the extinction coefficients of the individual passbands, which are listed in Table 1.

We have calculated the empirical stellar locus for our selected GS2, GSV, GM2 and GMV multiband catalogues, respectively. For each catalogue, we select reference samples respectively for the LMC, SMC and MW stars to obtain their stellar locus. We require that reference sample stars have photometric errors in all bands smaller than 0.05 mag and have low line-of-sight extinction from the extinction map of Schlegel, Finkbeiner & Davis (1998, SFD hereafter). The upper limits of the extinction vary from  $E(B - V)_{\max} = 0.030$  mag to 0.055 mag for the individual reference samples to obtain enough stars. In Table 2 we list the extinction upper limit  $E(B - V)_{\max}$  and the star counts  $N$  of all the reference samples. The reddening effects of the reference stars are corrected using the extinction values from the SFD map and the reddening coefficients from Table 1. In the current work, we assume the intrinsic colour  $(g - K_S)_0$  as the independent variable and use fifth-order polynomials to fit the running medians of the individual colours to obtain the stellar locus. The lower and upper  $(g - K_S)_0$  limits [ $(g - K_S)_{0,\min}$  and  $(g - K_S)_{0,\max}$ ] of all the reference samples are also presented in Table 2. As an example, we show the example stellar locus resulted from the LMC reference sample of the GMV catalogue in Fig. 4.

The best-fit intrinsic color  $(g - K_S)_0$  and reddening value  $E(B - V)$

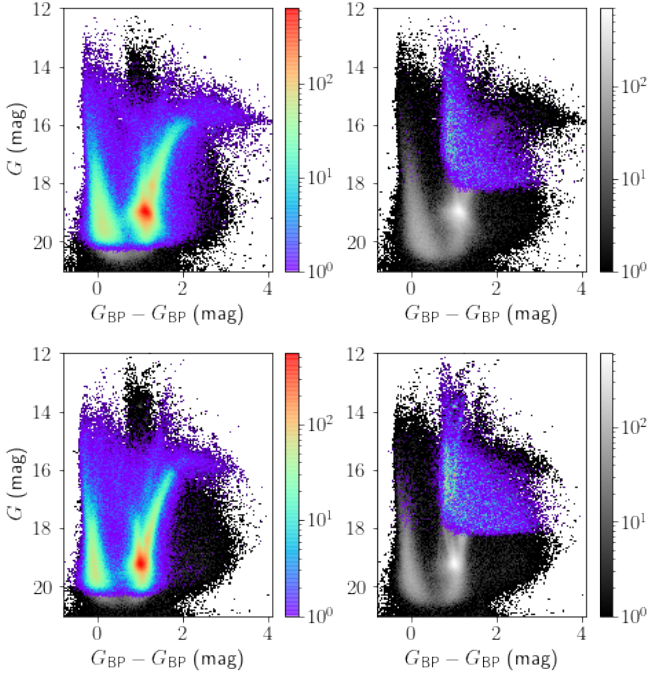


**Figure 3.** The Gaia  $G_{BP} - G_{RP}$  versus  $G$  CMDs of GMV catalogue stars in the LMC (upper panels) and SMC (bottom panels) regions. The background grey images show all stars in the corresponding area. The colour images in the left panels show the LMC (upper) and SMC (bottom) sources after the astrometric selection, respectively. The colour images in the right panels show the selected MW foreground sources in the corresponding area.

of a given star are found by minimizing  $\chi^2$  defined as

$$\chi^2 = \frac{1}{4} \sum_{i=1}^6 \left( \frac{c_{\text{obs}}^i - c_{\text{sim}}^i}{\sigma_i} \right)^2, \quad (2)$$

where  $c_{\text{obs}}^i$  are 6 observed colors ( $G_{BP} - G_{RP}$ ,  $g - r$ ,  $r - i$ ,  $i - J$ ,  $J - H$  and  $H - K_S$  for the GS2 and GM2 catalogues, and  $G_{BP} - G_{RP}$ ,  $g - r$ ,  $r - i$ ,  $i - Y$ ,  $Y - J$  and  $J - K_S$  for the GSV and GMV catalogues),  $c_{\text{sim}}^i$  and  $\sigma_i$  are the corresponding simulated colours and colour uncertainties, respectively. The colour uncertainties  $\sigma_i$  are the combination of the photometric uncertainties and stellar locus fitting errors.

The optimization is carried out by running a pseudo- $E(B - V)$  ranging from  $-0.1$  mag to  $E(B - V)_{\text{SFD}} + 0.1$  mag in step of  $0.002$  mag and  $(g - K_S)_0$  ranging from  $(g - K_S)_{0,\text{min}}$  to  $(g - K_S)_{0,\text{obs}} + 0.1$  mag in step of  $0.01$  mag, where  $E(B - V)_{\text{SFD}}$  is the reddening value of a star from the SFD map and  $(g - K_S)_{0,\text{obs}}$  is the observed colour values. If the value of  $(g - K_S)_{0,\text{obs}} + 0.1$  is larger than  $(g - K_S)_{0,\text{max}}$ , we will adopt  $(g - K_S)_{0,\text{max}}$  as the maximum value of the pseudo- $(g - K_S)_0$ . As the reddening values in the MCs area are relatively low, we have set a negative lower limit of the reddening values to avoid the systematically overestimation of reddening values for regions of low extinction (Berry et al. 2012; Schlafly et al. 2014; Chen et al. 2014, 2015).

As shown in Fig. 9 of Berry et al. (2012), the intrinsic colour and reddening degeneracy can be broken when we combine the optical and the near-IR colours. However, due to the photometric errors and the fact that the stellar locus orientation in the near-IR bands is not perpendicular to the reddening vectors, the covariance between the best-fit intrinsic colours  $(g - K_S)_0$  and reddening  $E(B - V)$  values

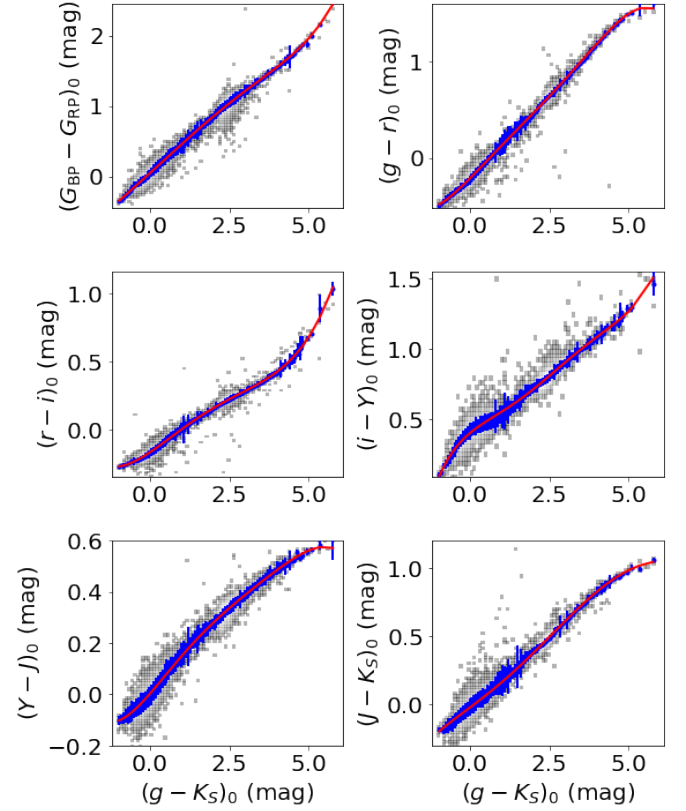


**Figure 4.** Colour-colour diagrams of all stars from the LMC reference sample of the GMV catalogue. The background grey contours are on a logarithmic scale. Blue points and error bars represent the median values and standard deviations of the colours for the individual  $(g - K_S)_0$  bins. The Red lines are the fifth polynomial fits to the median values.

does not vanish. We have simulated the GMV colours of fiducial stars in the LMC based on our derived stellar locus. We assume different intrinsic colours  $(g - K_S)_0 = 0.5$  and  $3.0$  mag, representing blue and red stars, respectively. We set the reddening value  $E(B - V) = 0.5$  mag. By adopting three sets of photometric errors,  $0.02$ ,  $0.05$  and  $0.08$  mag, the ‘observed’ colours of the fiducial stars are generated. For each star, we randomly generate their colours and calculate the best-fit parameters  $(g - K_S)_0$  and  $E(B - V)$  by our SED fitting algorithm 1000 times. The distributions of the best-fit parameters are shown in Fig. 5. Overall, our algorithm is able to recover robust values of  $(g - K_S)_0$  and  $E(B - V)$  for both the blue and stars. Similar as in the work of Berry et al. (2012) and Chen et al. (2014), the  $(g - K_S)_0$  and  $E(B - V)$  covariance is larger for a blue star than a red one. For a star with larger photometric errors, the covariance is larger. For the three assumed cases of photometric errors,  $0.02$ ,  $0.05$  and  $0.08$  mag, the dispersions of reddening  $E(B - V)$  values are  $0.09$ ,  $0.21$  and  $0.26$  mag, respectively, for the blue star, and  $0.05$ ,  $0.16$  and  $0.23$  mag, respectively, for the red star.

We have also investigated the covariance between the stellar intrinsic colour  $(g - K_S)_0$  and the reddening  $E(B - V)$  values for real stars in our sample. The resultant  $\chi^2$  surfaces for four example blue and red stars in both the LMC and SMC samples are illustrated in Fig. 6. The covariance between the stellar intrinsic colour  $(g - K_S)_0$  and the reddening  $E(B - V)$  values of the stars in the MCs is very similar to that of the Galactic stars from the tests in Berry et al. (2012, their Fig. 12) and Chen et al. (2014, their Fig. 5). For all

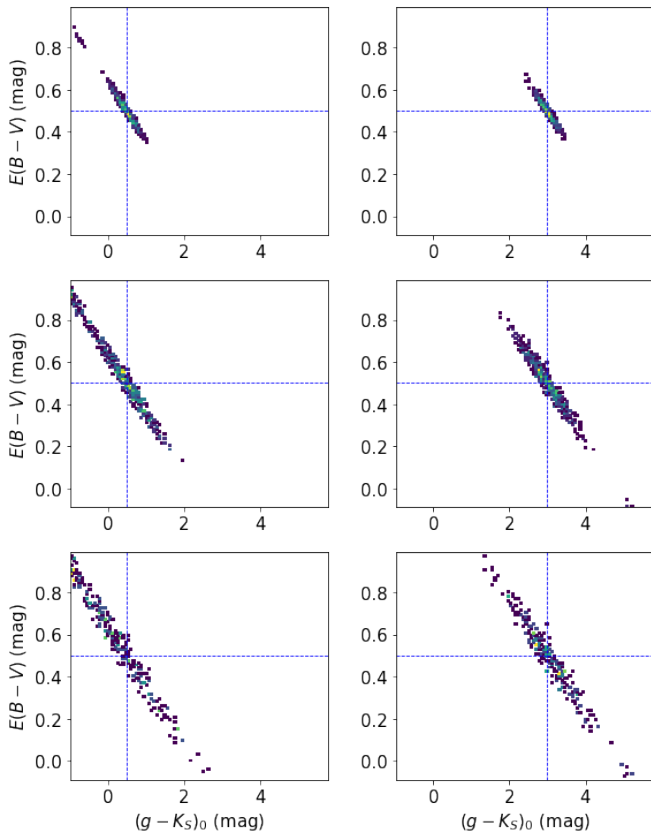


**Figure 5.** Monte Carlo simulations for two GMV fiducial stars in the LMC of intrinsic colours  $(g - K_S)_0 = 0.5$  (left panels) and  $3.0$  mag (right panels). Each panel shows the distribution of the best-fit results in the  $(g - K_S)_0$  and  $E(B - V)$  plane. The upper, middle and bottom rows refer to the results of the assumed photometric errors of  $0.02$ ,  $0.05$  and  $0.08$  mag, respectively. The two dashed lines in each panel mark the assumed  $(g - K_S)_0$  and  $E(B - V)$  values of the stars.

the four example stars, the  $\chi^2$  distributions always possess only one peak. The  $E(B - V)$  versus  $(g - K_S)_0$  covariance of the stars in the LMC is very similar to that of the stars in the SMC, and it does not strongly depend on the reddening  $E(B - V)$  values. These features indicate that our  $\chi^2$  minimization SED fitting algorithm produces statistically correct results. With the combination of the optical and near-IR photometries, we are able to break the degeneracy between the intrinsic stellar colour and the dust reddening.

### 3.3 Construction of high-resolution reddening maps

Based on the reddening estimates of the individual stars, we are then able to map the dust reddening distributions of the MCs. We use the HEALPix pixelization scheme (Górski et al. 2005) as our method to divide the sky into individual subfields (pixels). In the current work, we have adopted a variable resolution based on stellar density. We require that there are at least 20 stars in each pixel. The resolution of the pixels varies from  $\sim 26$  arcsec (with HEALPix  $n_{\text{side}} = 8,192$ ) to  $\sim 55$  arcmin (with HEALPix  $n_{\text{side}} = 64$ ). For each pixel, we first exclude outliers that have reddening values outside the  $3\sigma$  limit. The average and variance of the reddening values of the remaining stars are respectively adopted as the reddening value and the reddening uncertainty of the pixel.

## 4 RESULT

We have applied our SED fitting algorithm to the individual sample stars. In the current work, we exclude the bad SED fits with a minimum  $\chi^2$  larger than 2. This yields a total number of 4,037,497 stars in our final catalogue, including  $\sim 1.9$  million LMC stars, 1.5 million SMC stars and 0.6 million MW stars.

### 4.1 Reddening maps of the MCs

The LMC and SMC stars in our final catalogue are used to construct the high resolution reddening maps of the MCs, which are plotted in Fig. 7. Our reddening maps cover about  $360 \text{ deg}^2$  sky area toward the MCs. The average reddening value is  $E(B - V) = 0.07$  mag in the LMC area and  $E(B - V) = 0.04$  mag in the SMC area. In the LMC area, the reddening values increase and exceed  $E(B - V) = 0.38$  mag in the region of the famous CO arc cloud (RA  $\sim 87.0^\circ$  and Dec  $\sim -70.1^\circ$ ; Dobashi et al. 2008). In the SMC area, the reddening values increase and reach its maximum value with  $E(B - V) = 0.2$  mag in the region of the SMC southwestern bar (RA  $\sim 11.56^\circ$  and Dec  $\sim -73.25^\circ$ ). Some ‘stripelike’ structures are visible in the reddening map, especially for the region toward the SMC. This is caused by the lack of observations in the gaps between the VMC fields.

Thanks to the large size of our stellar sample, we are able to achieve very fine resolutions and capture the fractal dust in very good detail, especially in the regions toward the LMC and SMC centre. The angular resolution of our resultant map is displayed in Fig. 8. The resolution of the reddening map is  $\sim 26$  arcsec in the central parts of the LMC and SMC, and decreases down to  $\sim 55$  arcmin in the MCs outskirts. The typical resolution of our map is  $\sim 1.7$  arcmin.

Our reddening maps can be accessed at <http://paperdata.china-vo.org/diskec/mcdust/mcmap.fits>.

To use our maps, we provide a simple PYTHON procedure in our Github project ([https://github.com/helongguo/MCdustmaps\\_chen2021](https://github.com/helongguo/MCdustmaps_chen2021)), which returns reddening values for input positions (RA and Dec). A simple example of how to use the procedure is also given in the project. The final catalogue containing the best-fit values of  $E(B - V)$  from our SED fitting of  $\sim 4$  million stars, is publicly available via:

<http://paperdata.china-vo.org/diskec/mcdust/starebv.fits>.

Finally, we note that our reddening maps are two-dimensional (2D) maps, which lack the distance information. In Fig. 9 we plot the distributions of the reddening values of stars in a example pixel of the SMC. The distribution of reddenings along the example line-of-sight is bimodal. If we assume that all the dust reddening in the region comes from a relatively thin (comparing to the stellar disk) layer of dust along the line of sight. We can thus assume that stars either experience all of the dust column, or none of it. The probability distribution of the reddening values then becomes bimodal. As shown in the Figure, due to the limited depths of our adopted photometric data, there are more stars in our sample that lie in front of the dust layer than those lie behind. Our algorithm, which calculates the average reddening value of the pixel after excluding the outliers, tends to present the reddening values of stars in front of the dust layer. Thus for stars embedded or behind the dust layer, values from our reddening maps may be underestimated.

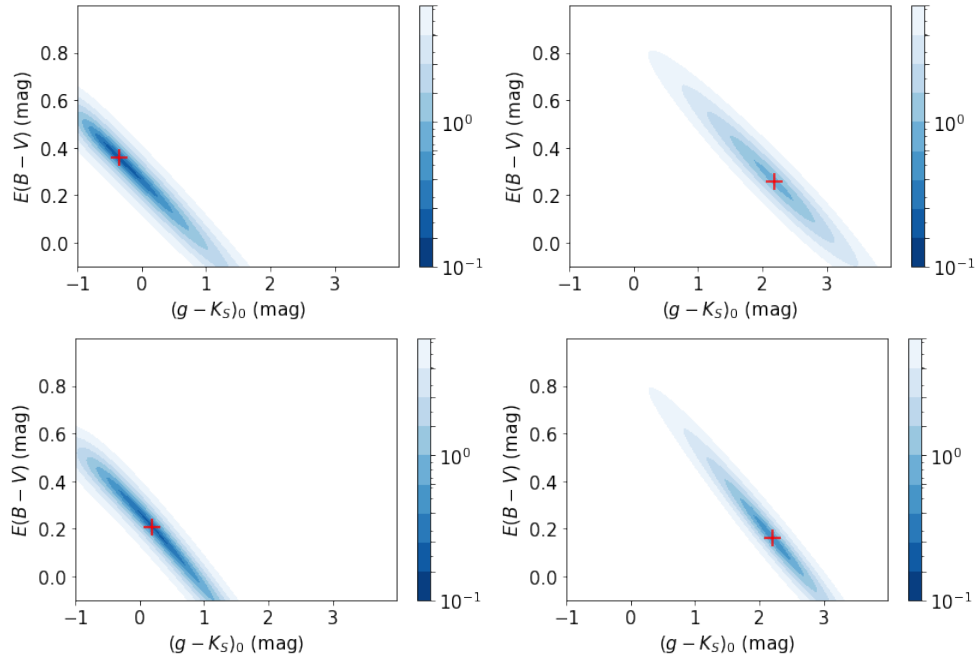


**Figure 6.** The  $\chi^2$  surfaces for four example stars in the GMV catalogue (upper left: a blue star in the LMC, upper right: a red star in the LMC, bottom left: a blue star in SMC, and bottom right: a red star in the SMC). For all panels, the best-fitted  $(g - K_S)_0$  and  $E(B - V)$  values are marked with red pluses.

## 4.2 The MW foreground reddening maps of the area toward the MCs

The resultant reddening maps as shown in Fig. 7 are calculated from the stars belonging to the MCs, which present the integrated dust reddening along the lines of sight. They are important tools for the reddening correction of sources in the MCs. However, to study the dust distribution in the LMC and SMC galaxies, we need to remove the MW foreground dust contamination. Based on our selected MW sample stars, we have constructed the MW foreground reddening maps of the sky area toward the MCs, which are plotted in Fig. 10. In the regions toward the MCs, the MW foreground dust show inhomogeneous clumpy features. Dust clouds can be visible in the south of the LMC disk (RA  $\sim 60^\circ - 105^\circ$  and Dec  $\sim -73^\circ$ ) and in the east of the SMC disk (RA  $\sim 20^\circ - 30^\circ$  and Dec  $\sim -75^\circ$ ), where the typical reddening value could be  $E(B - V) \sim 0.15$  mag. The average reddening values of the foreground MW dust is  $E(B - V) = 0.06$  mag in the LMC region and 0.04 mag in the area toward the SMC.

## 4.3 Local dust distributions of the LMC and the SMC

Finally, we subtract the MW foreground dust contamination (Fig. 10) from the reddening maps of the MCs as shown in Fig. 7 and obtain the local dust distributions of the LMC and SMC galaxies, which are shown in Fig. 11.

Fig. 11 represents the very first high angular resolution local dust reddening maps of the LMC and SMC galaxies. Overall, the dust in the LMC and SMC are mainly located in the disk regions of the galaxies. The previously known molecular clouds such as the 30 Dor complex (RA =  $5^{\text{h}}38^{\text{m}}38^{\text{s}}$ , Dec =  $69^\circ 5'.07$ ), LMC-114 (RA =  $5^{\text{h}}23^{\text{m}}$ , Dec =  $68^\circ$ ; Fukui et al. 2008) and LMC-154 (RA =  $5^{\text{h}}32^{\text{m}}$ , Dec =  $68^\circ 30'$ ; Fukui et al. 2008) are clearly visible. The local dust maps of the LMC and SMC galaxies show very similar features to the spatial structures of the LMC and SMC that traced by the young stars in

the previous works (e.g. Fig. A.6 and Fig. A.7 of Gaia Collaboration et al. 2021b), which suggests the robustness of our result.

## 5 DISCUSSION

### 5.1 Comparison of reddening values of the individual stars from different samples

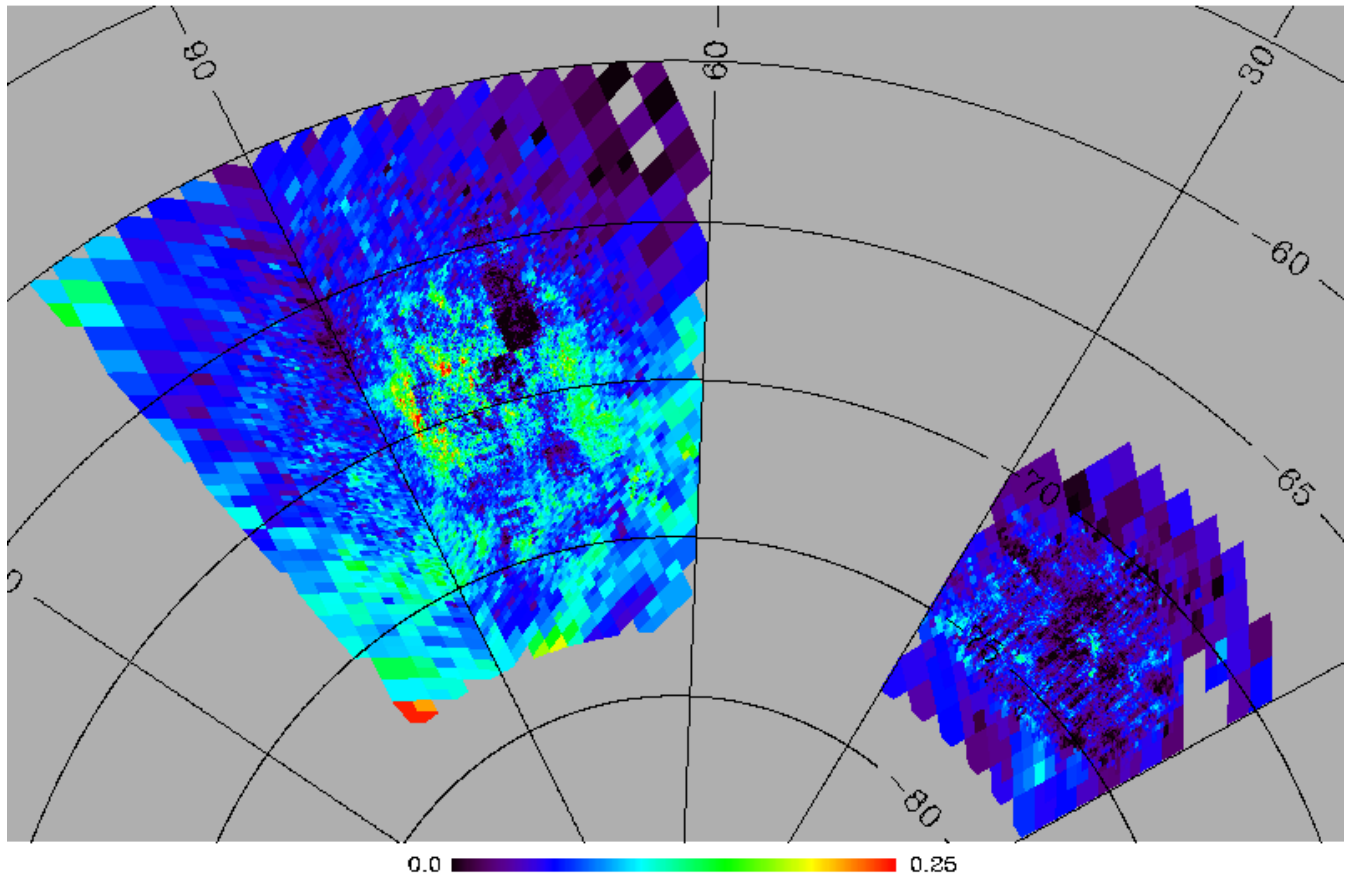
We have selected four multi-band photometric samples (i.e. the GSV, GS2, GMV and GM2 catalogues) from the optical and near-IR survey catalogues and applied our SED algorithm to the four catalogues independently. There are common stars in the four catalogues and their reddening values have been calculated more than once. These common stars provide an opportunity to examine the precision of reddening values delivered by our SED method. We plot the distribution of the differences of reddening values deduced from the common stars from different samples in Fig. 12. There are no systematic offsets. The internal precision of our resultant reddening values, which can be estimated by the dispersions of  $\Delta E(B - V)$  divided by a square root of 2, is about 0.04 mag.

### 5.2 Comparison of reddening values of the individual stars with previous work

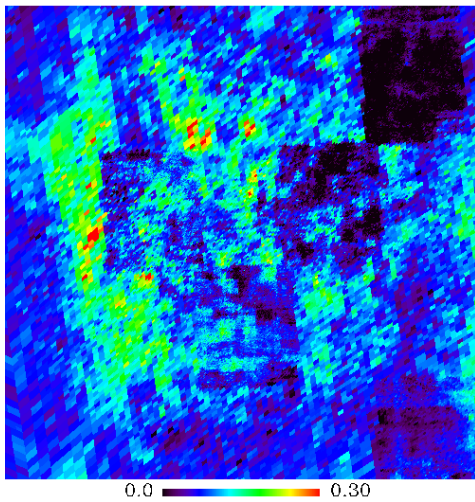
We have also compare our derived reddening values with measurements from Guo et al. (2021). Values of  $r$ -band extinction of over 17 million stars in the southern sky are provided by Guo et al. (2021), which are obtained by SED fitting to photometric measurements from the SMSS DR1, 2MASS, the Wide-Field Infrared Survey Explorer (WISE; Wright et al. 2010) and Gaia DR2.

The comparison result is shown in Fig. 13. We cross-match our results with those of Guo et al. (2021) with a matching radius of 2 arcsec and obtain 315 common stars. The values of  $A_r$  in Guo et al. (2021) are converted to  $E(B - V)$  values by  $E(B - V) = 0.43 \times A_r$ ,



MCs  $E(B-V)$  (mag)

LMC centre



SMC centre

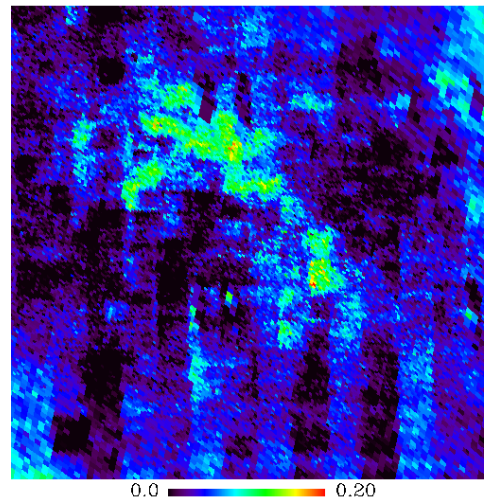


**Figure 7.** The reddening maps of the MCs. The bottom panels show the zoomed maps toward the LMC (left) and the SMC centre (right), respectively.



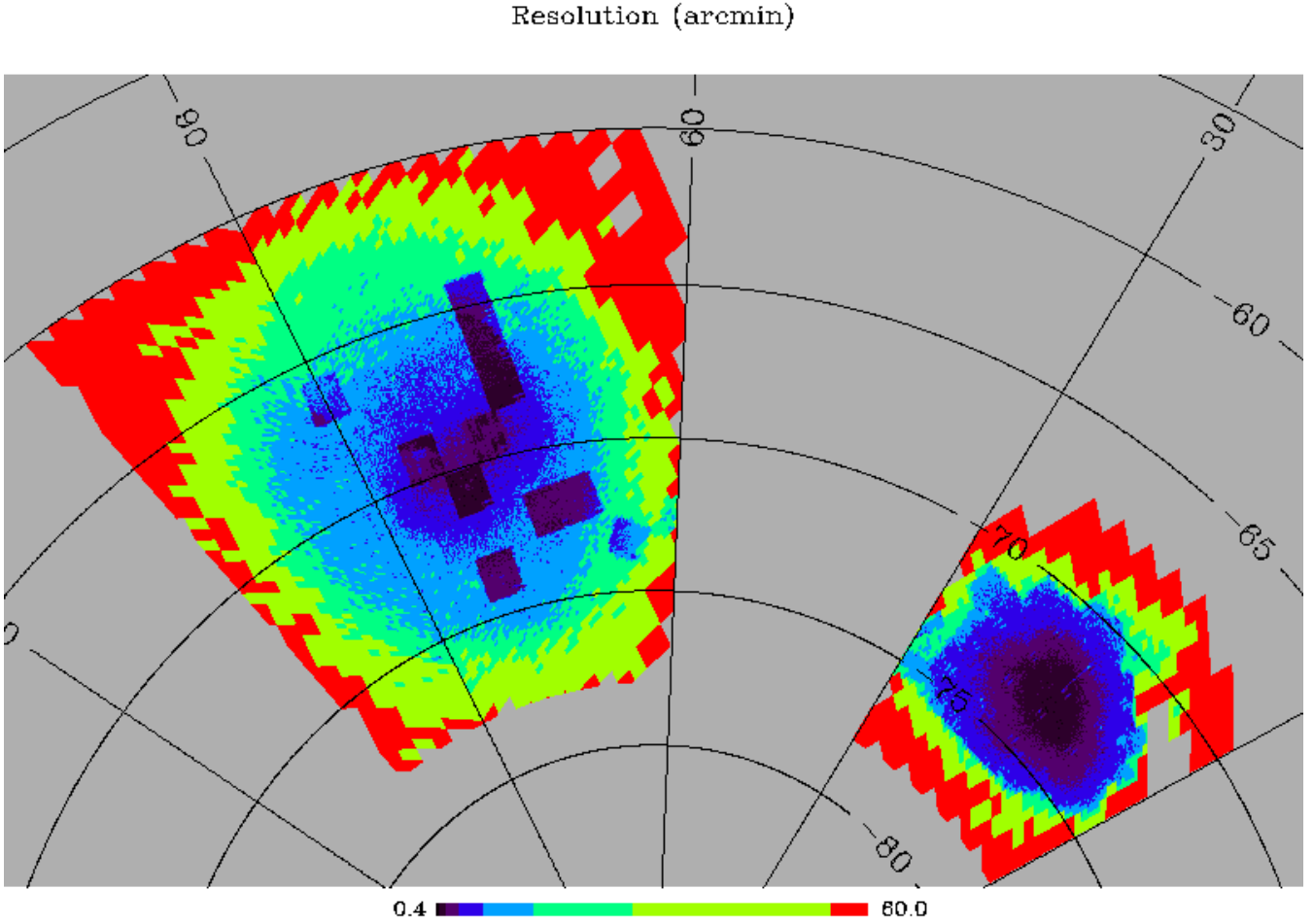


**Figure 8.** The angular resolution of our reddening maps.

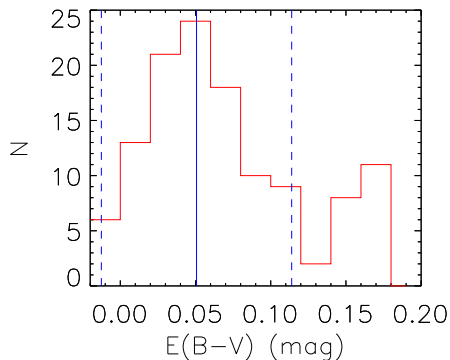


**Figure 9.** The distribution of reddening values for all stars in an example subfield (pixel) of the SMC. The vertical blue solid and dashed lines represent our resultant reddening value and the reddening uncertainty of the pixel.

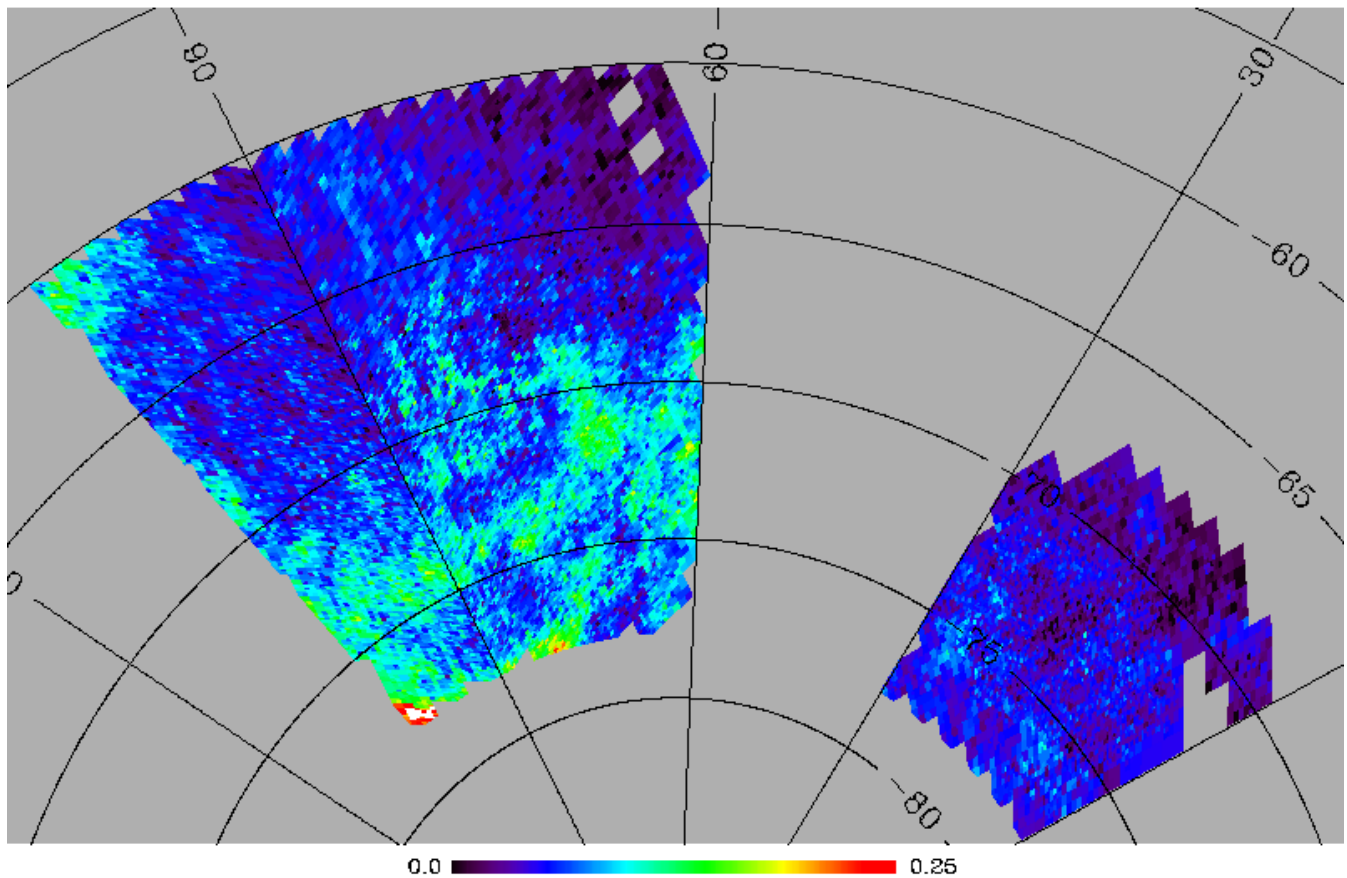
(Yuan et al. 2013). Our measurements are in good agreement with those from Guo et al. (2021). The resulted differences have a small offset of 0.027 mag and a small rms scatter of 0.064 mag.

### 5.3 Comparisons of reddening maps with previous works

Here we compare our reddening maps with several other recent studies, including,

- (i) the reddening maps from Haschke et al. (2011), which are obtained from the  $E(V - I)$  reddening values of red clump and RR Lyrae stars selected from the data of OGLE-III,
- (ii) the reddening maps from Joshi & Panchal (2019), which are obtained from the  $E(V - I)$  reddening values of classical Cepheid variables selected from the data of OGLE-IV,
- (iii) the reddening maps from Górski et al. (2020), which are obtained from the reddening values of red clump stars selected from the data of OGLE-III,
- (iv) and the reddening maps from Skowron et al. (2021), which are obtained from the reddening values of red clump stars selected from the data of OGLE-IV.

Since the angular resolution of our reddening map is higher than those of the previous works for most of the fields, we convert our map respectively to the same angular resolutions as the maps from the literature by 2D linear interpolations. The maps from the literature are all converted to  $E(B - V)$  using the relations recommended by the authors. We adopt the relation  $E(B - V) = 0.725 \times$

MW foreground  $E(B-V)$  (mag)

**Figure 10.** The MW foreground reddening maps of the sky area toward the MCs.

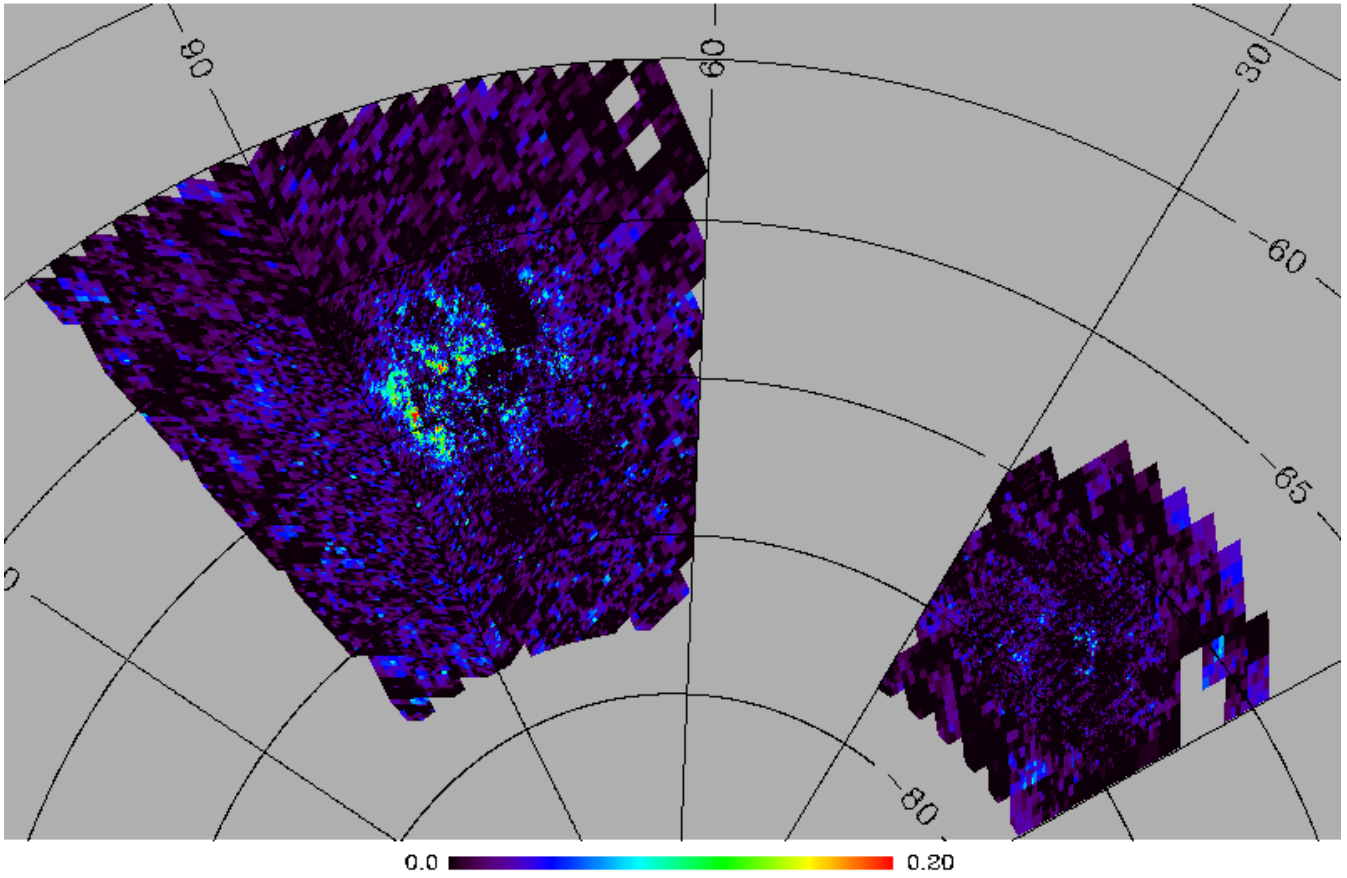
$E(V-I)$  for the maps of [Haschke et al. \(2011\)](#),  $E(B-V) = 0.758 \times E(V-I)$  for the maps of [Joshi & Panchal \(2019\)](#),  $E(B-V) = 0.759 \times E(V-I)$  for the maps of [Górski et al. \(2020\)](#), and  $E(B-V) = 0.808 \times E(V-I)$  for the maps of [Skowron et al. \(2021\)](#). The comparison results are shown Fig. 14. Overall, our resultant reddening maps are in good agreement with those of the previous works. The average differences are negligible between our maps and those from [Joshi & Panchal \(2019\)](#) and [Skowron et al. \(2021\)](#). The [Haschke et al. \(2011\)](#) maps are systematically slightly smaller than our results, while the [Górski et al. \(2020\)](#) maps are slightly larger. The dispersions of the differences are small, with rms scatter of only  $\sim 0.03$  to  $0.04$  mag for all the maps.

## 6 CONCLUSION

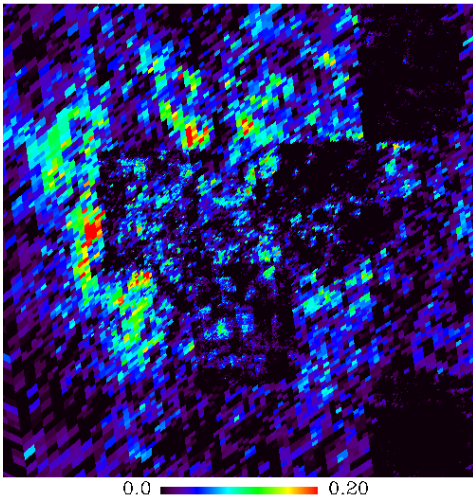
Based on the optical and near-IR photometries from Gaia EDR3, SMSS DR2, SMASH DR2, 2MASS PSC, VMC DR4 and VMC DR5.1, we have obtained four different multi-band photometric catalogues: the GS2, GSV, GM2 and GMV catalogue. The Gaia EDR3 astrometric measurements are used to select the clean LMC, SMC and MW stellar samples. A SED fitting algorithm is applied to the sample stars to calculate their reddening values. As a result, we

have obtained  $E(B-V)$  reddening values of  $\sim 1.9$  million stars in the LMC, 1.5 million stars in the SMC and 0.6 million stars in the MW. Based on the reddening values of the LMC and SMC stars, we have constructed high resolution reddening map of the MCs. The map has a resolution of  $\sim 26$  arcsec in the centre region of the MCs, and of  $\sim 55$  arcmin in the outskirts. The typical resolution is about 1.7 arcmin. Our resultant high-resolution reddening map is available online ([https://github.com/helongguo/MCdustmaps\\_chen2021](https://github.com/helongguo/MCdustmaps_chen2021)), which should be quite useful for reddening correction of sources in the MCs.

Based on the reddening values of the MW stars, we have obtained the reddening distribution of the foreground MW dust, which are finally subtracted to obtain the local dust distributions of the LMC and SMC galaxies. The local dust map of the LMC and SMC show very similar features to the spatial structures of the LMC and SMC that are traced by the young stars. It should enable us to carry out a detailed, quantitative study of the structure and properties of dust in the two galaxies.

MCs local  $E(B-V)$  (mag)

LMC centre



SMC centre

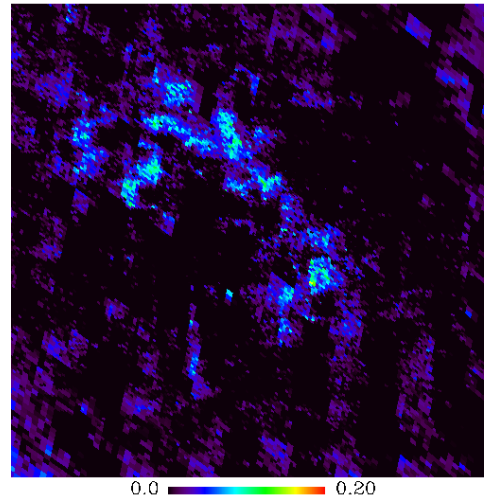


**Figure 11.** The local dust distributions of the LMC and SMC galaxies. The bottom panels show the zoomed local reddening maps of the LMC (left) and the SMC centre (right), respectively.



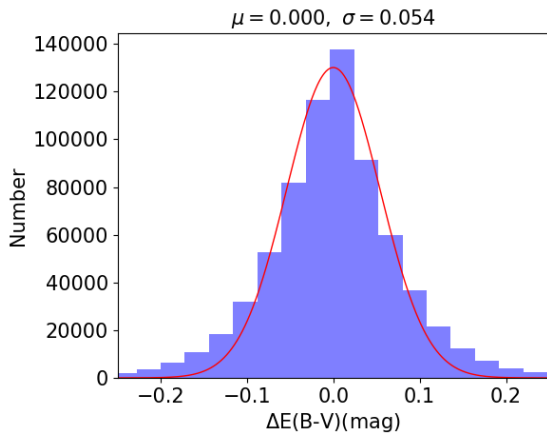


**Figure 12.** Histogram of differences of reddening values by common stars derived from different multiband photometric samples in the current work. A Gaussian fit to the distribution is overlotted, and the mean and dispersion of the Gaussian are marked in the diagram.

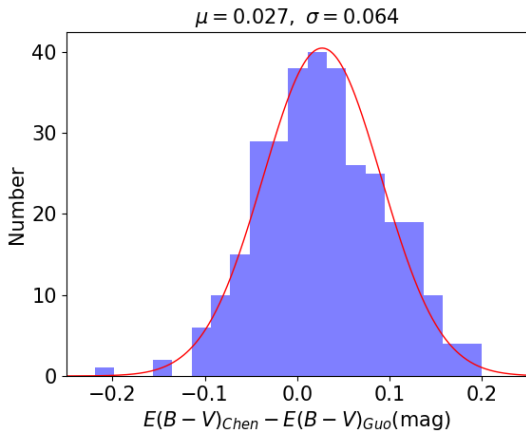


**Figure 13.** Histograms of differences of reddening values of the individual stars derived from the current work and those given by Guo et al. (2021). A Gaussian fit to the distribution is overlotted, and the mean and dispersion of the Gaussian are marked in the diagram.]

## ACKNOWLEDGEMENTS

This work is partially supported by the National Key R&D Program of China No. 2019YFA0405500, National Natural Science Foundation of China 12173034, 11803029, U1531244 and U1731308 and Yunnan University grant No. C176220100007. We acknowledge the science research grants from the China Manned Space Project with NO. CMS-CSST-2021-A09, CMS-CSST-2021-A08 and CMS-CSST-2021-B03.

This work presents results from the European Space Agency (ESA) space mission Gaia. Gaia data are being processed by the Gaia Data Processing and Analysis Consortium (DPAC). Funding for the DPAC is provided by national institutions, in particular the institutions participating in the Gaia MultiLateral Agreement (MLA). The Gaia mission website is <https://www.cosmos.esa.int/gaia>. The Gaia archive website is <https://archives.esac.esa.int/gaia>.

This publication makes use of data products from the Two Micron All Sky Survey, which is a joint project of the University of Massachusetts and the Infrared Processing and Analysis Cen-

ter/California Institute of Technology, funded by the National Aeronautics and Space Administration and the National Science Foundation.

This work is based on data products from observations made with ESO Telescopes at the La Silla or Paranal Observatories under ESO programme ID 179.B-2003.

The national facility capability for SkyMapper has been funded through ARC LIEF grant LE130100104 from the Australian Research Council, awarded to the University of Sydney, the Australian National University, Swinburne University of Technology, the University of Queensland, the University of Western Australia, the University of Melbourne, Curtin University of Technology, Monash University and the Australian Astronomical Observatory. SkyMapper is owned and operated by The Australian National University's Research School of Astronomy and Astrophysics. The survey data were processed and provided by the SkyMapper Team at ANU. The SkyMapper node of the All-Sky Virtual Observatory (ASVO) is hosted at the National Computational Infrastructure (NCI). Development and support of the SkyMapper node of the ASVO has been funded in part by Astronomy Australia Limited (AAL) and the Australian Government through the Commonwealth's Education Investment Fund (EIF) and National Collaborative Research Infrastructure Strategy (NCRIS), particularly the National eResearch Collaboration Tools and Resources (NeCTAR) and the Australian National Data Service Projects (ANDS).

This research uses services or data provided by the Astro Data Lab at NSF's National Optical-Infrared Astronomy Research Laboratory. NOIRLab is operated by the Association of Universities for Research in Astronomy (AURA), Inc. under a cooperative agreement with the National Science Foundation. This work is based on observations at Cerro Tololo Inter-American Observatory, National Optical Astronomy Observatory (NOAO Prop. ID: 2013A-0411 and 2013B-0440; PI: Nidever), which is operated by the Association of Universities for Research in Astronomy (AURA) under a cooperative agreement with the National Science Foundation.

## DATA AVAILABILITY

The data underlying this article are available in the article and in its online supplementary material.

## REFERENCES

- Abbott T. M. C., et al., 2018, *ApJS*, **239**, 18  
 Bailer-Jones C. A. L., 2011, *MNRAS*, **411**, 435  
 Berry M., et al., 2012, *ApJ*, **757**, 166  
 Bessell M. S., 2011, in Qain S., Leung K., Zhu L., Kwok S., eds, *Astronomical Society of the Pacific Conference Series Vol. 451, 9th Pacific Rim Conference on Stellar Astrophysics*. p. 323  
 Cardelli J. A., Clayton G. C., Mathis J. S., 1989, *ApJ*, **345**, 245  
 Chen B. Q., Schultheis M., Jiang B. W., Gonzalez O. A., Robin A. C., Rejkuba M., Minniti D., 2013, *A&A*, **550**, A42  
 Chen B. Q., et al., 2014, *MNRAS*, **443**, 1192  
 Chen B. Q., Liu X. W., Yuan H. B., Huang Y., Xiang M. S., 2015, *MNRAS*, **448**, 2187  
 Chen B. Q., et al., 2019, *MNRAS*, **483**, 4277  
 Choi Y., et al., 2018, *ApJ*, **866**, 90  
 Cioni M. R. L., et al., 2011, *A&A*, **527**, A116  
 Cohen M., Wheaton W. A., Megeath S. T., 2003, *AJ*, **126**, 1090  
 Dalton G. B., et al., 2006, in McLean I. S., Iye M., eds, *Society of Photo-Optical Instrumentation Engineers (SPIE) Conference Series Vol. 6269*,

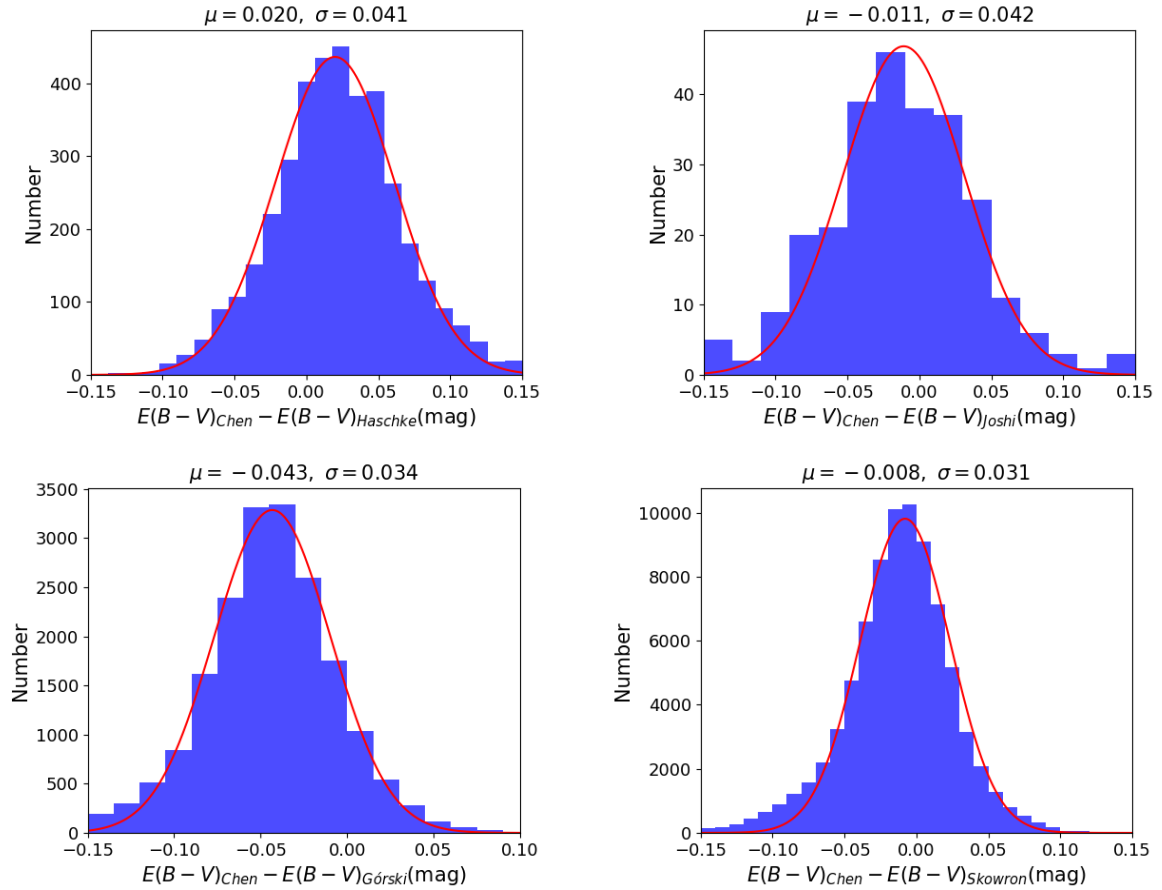


**Figure 14.** Histograms of differences of the reddening values of our reddening maps and those from [Haschke et al. \(2011\)](#), [Joshi & Panchal \(2019\)](#), [Górski et al. \(2020\)](#) and [Skowron et al. \(2021\)](#). Gaussian fits to the distributions are overplotted, and the mean and dispersion of the Gaussian are marked in each panel.

- Society of Photo-Optical Instrumentation Engineers (SPIE) Conference Series. p. 62690X, doi:10.1117/12.670018
- Deb S., 2017, arXiv e-prints, p. arXiv:1707.03130
- Dobashi K., Bernard J. P., Hughes A., Paradis D., Reach W. T., Kawamura A., 2008, *A&A*, **484**, 205
- Dobashi K., Bernard J.-P., Kawamura A., Egusa F., Hughes A., Paradis D., Bot C., Reach W. T., 2009, *AJ*, **137**, 5099
- Emerson J. P., Sutherland W. J., McPherson A. M., Craig S. C., Dalton G. B., Ward A. K., 2004, *The Messenger*, **117**, 27
- Flaugher B., et al., 2015, *AJ*, **150**, 150
- Fukui Y., et al., 2008, *ApJS*, **178**, 56
- Gaia Collaboration et al., 2021a, *A&A*, **649**, A1
- Gaia Collaboration et al., 2021b, *A&A*, **649**, A7
- Gordon K. D., Clayton G. C., Misselt K. A., Landolt A. U., Wolff M. J., 2003, *ApJ*, **594**, 279
- Górski K. M., Hivon E., Banday A. J., Wandelt B. D., Hansen F. K., Reinecke M., Bartelmann M., 2005, *ApJ*, **622**, 759
- Górski M., et al., 2020, *ApJ*, **889**, 179
- Green G. M., Schlafly E., Zucker C., Speagle J. S., Finkbeiner D., 2019, *ApJ*, **887**, 93
- Guo H. L., et al., 2021, *ApJ*, **906**, 47
- Harris J., Zaritsky D., Thompson I., 1997, *AJ*, **114**, 1933
- Haschke R., Grebel E. K., Duffau S., 2011, *AJ*, **141**, 158
- Inno L., et al., 2016, *ApJ*, **832**, 176
- Joshi Y. C., Panchal A., 2019, *A&A*, **628**, A51
- Keller S. C., et al., 2007, *PASA*, **24**, 1
- Nidever D. L., et al., 2017, *AJ*, **154**, 199
- Nidever D. L., et al., 2021, *AJ*, **161**, 74
- Onken C. A., et al., 2019, *PASA*, **36**, e033
- Pejcha O., Stanek K. Z., 2009, *ApJ*, **704**, 1730
- Riello M., et al., 2021, *A&A*, **649**, A3
- Rubele S., et al., 2012, *A&A*, **537**, A106
- Rubele S., et al., 2018, *MNRAS*, **478**, 5017
- Schlafly E. F., et al., 2014, *ApJ*, **786**, 29
- Schlegel D. J., Finkbeiner D. P., Davis M., 1998, *ApJ*, **500**, 525
- Schultheis M., et al., 2014, *A&A*, **566**, A120
- Skowron D. M., et al., 2021, *ApJS*, **252**, 23
- Skrutskie M. F., et al., 2006, *AJ*, **131**, 1163
- Soszyński I., et al., 2009, *Acta Astron.*, **59**, 1
- Subramaniam A., 2005, *A&A*, **430**, 421
- Subramaniam S., Subramaniam A., 2012, *ApJ*, **744**, 128
- Tatton B. L., et al., 2013, *A&A*, **554**, A33
- Udalski A., Szymanski M., Kubiak M., Pietrzynski G., Soszynski I., Wozniak P., Zebrun K., 2000, *Acta Astron.*, **50**, 307
- Udalski A., Szymański M. K., Szymański G., 2015, *Acta Astron.*, **65**, 1
- Wright E. L., et al., 2010, *The Astronomical Journal*, **140**, 1868
- Yang M., et al., 2019, in *Supernova Remnants: An Odyssey in Space after Stellar Death II*. p. 93
- Yang M., et al., 2021, *A&A*, **646**, A141
- Yuan H. B., Liu X. W., Xiang M. S., 2013, *MNRAS*, **430**, 2188
- Zaritsky D., Harris J., Thompson I., 1997, *AJ*, **114**, 1002
- Zaritsky D., Harris J., Thompson I. B., Grebel E. K., Massey P., 2002, *AJ*, **123**, 855
- Zaritsky D., Harris J., Thompson I. B., Grebel E. K., 2004, *AJ*, **128**, 1606